

Computational Aeroelastic Simulation of Rapidly Morphing Air Vehicles

Evgeny Selitrennik* and Moti Karpel†

Technion—Israel Institute of Technology, 32000 Haifa, Israel

and

Yuval Levy‡

Israeli Computational Fluid Dynamics Center, 38900 Caesarea Industrial Park, Israel

DOI: 10.2514/1.C031041

A new approach for computational fluid dynamics-based aeroelastic simulation of rapidly morphing flight vehicles is presented. The morphing vehicle consists of a number of components interconnected by actuators and contact constraints. Due to aerodynamic, inertial, and actuation loads, the overall structure undergoes large-displacement morphing. The method assumes that each component experiences large rigid-body displacements and small elastic deformations that are linear combinations of the individual normal modes. The structural equations of motion are based on the fictitious-mass substructure modal synthesis method, which is expanded to allow large rotations between the structural components while keeping displacements and rotation compatibility at the interface coordinates. The compatibility equations are time-dependent, and the inclusion of their time derivatives in the equations of motion introduces nonlinear dynamic effects. The resulting generalized-coordinate nonlinear matrix equations of motion are embedded in a time-accurate computational fluid dynamics code. The vector of generalized forces includes aerodynamic forces from the computational fluid dynamics solution as well as inertial and actuation forces. The computational process is demonstrated by two different wing–body configurations where the wings are rotating from parallel to perpendicular positions relative to the body. The morphing simulations demonstrate a robust and stable computational process that exhibits significant aeroelastic effects.

I. Introduction

MORPHING aircraft are flight vehicles that change their shape substantially to achieve better performance characteristics at different mission conditions. The advances in recent years in the technology of unmanned aerial vehicles (UAVs) motivated an increased interest to the morphing-aircraft development by the military and aircraft industries, which led to numerous sponsored research programs. The U.S.-sponsored Defense Advanced Research Projects Agency Morphing Aircraft Structures Program [1] is the most famous example in which requirements and tasks for future morphing military aircraft are defined. The program's final goal is to create small autonomous types of UAVs with combined roles.

Among the various types of morphing vehicles, the ones that are launched with folded wings that are unfolded in midair draw special attention. The rapid changes in the aerodynamic, structural, and control properties raise difficult questions regarding the stability, controllability, and structural integrity of such vehicles during the morphing process. Aeroelastic effects may be critically important when one attempts to answer these questions. Several approaches have been suggested for the modeling of the morphing process. Researchers from the U.S. Air Force Research Laboratory presented the integrated aeroelastic multibody morphing simulation tool [2,3], which is based on the ADAMS multibody dynamic code combined with vortex-lattice-method code for aerodynamic loads estimation, and the Matlab/Simulink software package for automatic control modeling. The structural model of each substructure is created

separately using the MSC/NASTRAN code, and the structural model of the whole structure is created using the Craig–Bampton component mode synthesis process [4] with the interface constraints applied in a static manner. Ameri et al. [5] presented a morphing simulation that is implemented within the Matlab/Simulink environment based on mechanical interface of rigid components and inviscid quasi-steady vortex-lattice aerodynamics. Obradovic and Subbarao [6] presented a methodology for a six-degrees-of-freedom simulation of morphing aircraft that combines concurrent unsteady vortex-lattice aerodynamic forces and nonlinear equations of motion. The morphing dynamics are explicitly taken into account, resulting in additional body-frame forces and moments. The flexibility of the aircraft structure and the actuator dynamics are not included. Liu et al. [7] presented a nonlinear-aerodynamic–nonlinear-structures interaction methodology for continuous dynamic simulations of morphing-wing structures. The methodology combines the structural equations of motion in generalized modal coordinates, which are solved separately for each substructure, with the addition of the nonlinear stiffness coefficients, and an in-house computational fluid dynamics (CFD) solution. The interfaces between the substructures are assumed to be rigid with force, moment, and kinematic compatibilities applied at single interface points. Seigler et al. [8] presented a general model of morphing aircraft structures, based on a multibody dynamics formulation using Lagrange's equations. The aerodynamic forces applied on each substructure are represented as concentrated forces and moments acting on the center of mass. Tang and Dowell [9] presented a flutter investigation for a Z-shaped morphing wing. Each wing substructure was considered as a flat plate with free–free or clamped–free (for the part of the wing attached to the fuselage) boundaries. The hinges between the wing substructures were modeled as a number of torsion springs. The classical Rayleigh–Ritz approach was used for representing the displacements of each wing component. The expression for potential energy of the wing is derived as a sum of potential energies of all the wing components and all the torsion springs, with the displacements of all the substructures transformed into a central-body coordinate system. The aerodynamic loads were calculated using the vortex-lattice method. The equations of motion are derived using Lagrange's equations.

A key feature of a modal-based dynamic morphing simulation is the modal synthesis method that allows building the structural model

Presented as Paper 2010-2793 at the 51st AIAA/ASME/ASCE/AHS/ASC Structures, Structural Dynamics, and Materials Conference, Orlando, FL, April 12–15, 2010; received 27 March 2010; revision received 25 February 2012; accepted for publication 4 March 2012. Copyright © 2012 by Evgeny Selitrennik, Moti Karpel and Yuval Levy. All rights reserved. Copies of this paper may be made for personal or internal use, on condition that the copier pay the \$10.00 per-copy fee to the Copyright Clearance Center, Inc., 222 Rosewood Drive, Danvers, MA 01923; include the code 0021-8669/12 and \$10.00 in correspondence with the CCC.

*Graduate Student, Faculty of Aerospace Engineering.

†Professor, Sanford Kaplan Chair for Aerospace Engineering, Faculty of Aerospace Engineering, Fellow AIAA.

‡CEO, Senior Member AIAA.

from the modes of distinct structural components called substructures. According to [10], two approaches exist for construction of the structural model from the modes of distinct components called substructures: the dynamic-impedance and the dynamic-admittance approaches. In the dynamic-impedance approach, the behavior of the substructure is represented as a superposition of constrained modes describing the static behavior of the boundaries and clamped vibration modes obtained when fixing the boundaries. An example of such approach is the Craig–Bampton method [4]. In the dynamic-admittance concept, the dynamic behavior of the subcomponent is represented by its free–free vibration modes with the addition of the residual flexibility correction, which provides an exact representation of the boundaries’ static behavior. Such a method corresponds to the McNeal–Rubin method [11]. Several forms of substructuring methods for analyzing multibody systems are listed in [10].

The approach presented in this paper bases the dynamic equations of motion of the morphing structure on substructure normal modes using the fictitious-mass (FM) substructure synthesis method of Karpel and Newman [12] and Karpel and Raveh [13], where the component modes are generated with the interface coordinates loaded with large fictitious masses. Then, all the substructures are brought together, the fictitious masses are removed from the combined mass matrix, and the compatibility conditions are applied to connect between the structural components. The fictitious masses introduce local modes that produce effects similar to those of the constrained Craig–Bampton modes or the McNeal–Rubin residual flexibility, in a single set of component modes. The previous studies indicated that, the fictitious masses should be similar to the inertia properties of the entire structure. Solutions with various sets of fictitious masses showed that the results are insensitive to the mass magnitude, providing that they are large enough to cause significant near-boundary deformations and not large enough to cause numerical ill conditioning. The method is extended in this work to allow large rotations between the structural components while dynamically keeping the interface displacement and rotation compatibility constraints.

Computational aeroelasticity procedures can be categorized by the way the structural and aerodynamic models exchange information during the solution process [14,15]. Strongly coupled approaches are based on the simultaneous solution of structural and fluid equations as one system [16,17]. This approach is rarely used because there are many difficulties in solving both fluid and structural systems without significant simplifications of one of them. Most schemes solve the two systems in parallel with information exchanged in each time steps. The staggered algorithms [16,18], for example, allow parallel solutions using different CFD and structural dynamic codes. The closely coupled approach used in our work [19–21] solves the flowfield and the linear structural equations within the EZNSS CFD solver.

However, it should be clear that the emphasis of the present work is on the modal coupling process and on how to handle unsteady aerodynamic loads during morphing motions. Hence, inviscid aerodynamics was used in the paper, and details of the validation of the aerodynamic solver can be found in [22].

II. Approach Overview

The purpose of the paper is to introduce a new morphing simulation technique that combines CFD and structural dynamics techniques to analyze continuous morphing processes, including aerodynamic loads, structural response, relative intercomponent movements, and rigid-body motion of entire vehicles. The morphing deformations are limited to displacements of structural components that are interconnected by a specific set of points about which there are relative rotations between the components.

The structural displacements of the morphing flight vehicle at any intermediate position are assumed to be linear combinations of component modes that are formulated by the FM substructure synthesis method [12,13]. The application of the FM method in this work requires new developments of the coupling equations, which expand the method to support large intercomponent rotations in addition to elastic displacements compatibility. The modal equations

of motion for multicomponent structure are derived on the basis of the expanded FM method with the addition of actuators and constraint forces.

The EZNSS code [22], a multizone Euler/Navier–Stokes flow solver, which uses Chimera grids with deformable meshes, was selected for the research. The derived modal equations of motion were embedded in the CFD code with techniques that were developed by Raveh et al. [20,21]. The EZNSS code provides a number of algorithms for flow solution: the Beam and Warming algorithm [23], the Steger–Warming flux-vector-splitting method [24], and approximate Riemann solvers such as Harten, Lax, van Leer and contact (HLLC) scheme [25], AUSM⁺-up [26–28], and Mach-number-based advection pressure splitting (MAPS) scheme [29]. Any of these schemes may be used to conduct the simulation. The limiter that was developed by Koren [30] is employed to suppress oscillation in the solution. Two important features of the code are pivotal with regard to the current work. The first is the Chimera suite of routines that is embedded in the code, and the second is the dual-time-stepping time-integration procedure. In the Chimera overset grid approach [31,32], a separate computational mesh is generated for each component, such as the fuselage or the wing of an aircraft, separately. An outer mesh is generated so that it fully includes the meshes of all the components. The domain decomposition in this approach is simplified, and the number of zones that are required is substantially lower. However, the generation of grids surrounding each component is performed independently, and therefore points of a certain mesh may be located within the solid boundaries of the geometry. Regions located within solid boundaries are called “holes” [31]. This is treated by excluding points that are in the holes from the solution process and using interpolations to update the edges of the holes. The calculations to determine the holes and hole boundaries require a considerable computational effort that, in moving-body simulations, has to be added to the overall computational cost. The Chimera grid approach has two significant advantages when used for morphing simulations. First, the suite of Chimera routines embedded in the CFD code automatically facilitates an updated computational mesh after each shape change. Second, deformation of each structural component affects only the corresponding CFD mesh, while aerodynamic effects on other components are treated by the regular intermesh procedures.

The dual-time-step formulation [33] has an increased importance when conducting morphing or aeroelasticity simulations. Because the geometry changes require that the suite of Chimera routines for hole cutting and interpolation point search is invoked for each time step, using a regular time-accurate simulation, with a much smaller time step, becomes inefficient. The dual-time-step formulation allows the use of much larger time steps, and therefore the overhead of the Chimera routines and other routines, such as metric coefficient calculations, is greatly reduced. This is true even when a rather large number of subiterations is required for each time step to converge.

The aeroelastic simulation starts from a steady converged flow solution of the initial configuration. Each step in the simulation process starts with a CFD step. Then, the aerodynamic loads are transferred into generalized forces using

$$\{F_s\} = [\phi_{EA}]^T \{F_A\} \quad (1)$$

where $[\phi_{EA}]$ is the matrix of modal displacements in the aerodynamic grid calculated from the structural vibration modes using the infinite-plate-spline method [34] for lifting surfaces and the beam-spline method [35] for slender bodies. The spline transformations for the lifting surfaces were built using the upper skin deflections only, assuming insignificant local thickness changes. The inertial forces, which are calculated in the rotational frames of reference of every moving substructure, are also transferred into a generalized form. Then the solution of the modal equations of motion is advanced by the same time interval that is used for the flow solution using a time-marching scheme, such as Runge–Kutta or Adams–Bashforth [36]. Finally, the CFD grids are deformed to match the updated shape of the flight vehicle. This is used using the arc-length transfinite interpolation approach [37]. These steps are performed successively until a user-defined stop criterion is satisfied.

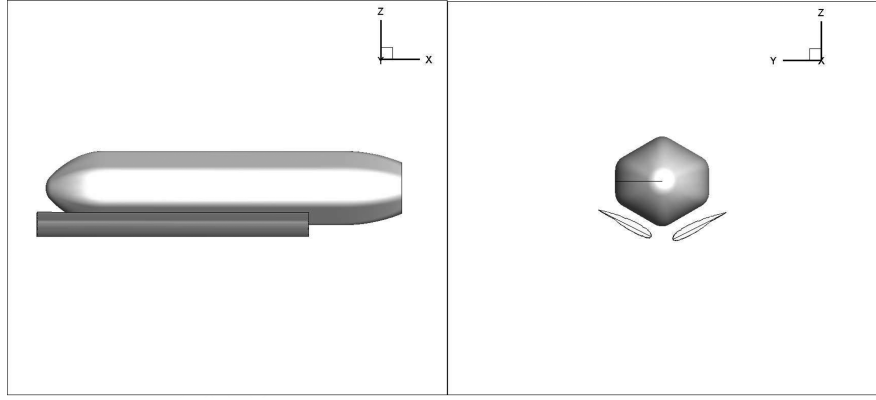


Fig. 1 Example 1 geometry with folded wings.

The computational process is demonstrated for the two models shown in Figs. 1–3. The first model (example 1) is of a two-wings-and-body configuration, where the wings are rotated rapidly from a parallel position along a fuselage to a perpendicular position. The second model (example 2) is of a wing–body configuration where the wing is rotating about a hinge attached to a slender body from a parallel position to a perpendicular one.

III. Coupling Equations

A typical morphing vehicle is an assembly of a central body and other components, such as wings, which are connected to the body and/or other components. The structure is assembled in several stages. In stage 1, wings are connected to the body in up to six time-variable interface displacement and rotation constraints per wing. A wing may rotate relative to the body around an axis that passes through the contact points. If there are other wings, stage 2 is performed with the product of stage 1 considered as a central body to which more wings are attached. If necessary, this expansion is repeated until each wing is connected to a parent component. Stage 3 may add actuators or structural elements that connect any two points

in the assembled structure. This assembly process can provide the basis for the equations of motion of any morphing structure where components move relative to each other.

A component is represented in the assembled equations of motion by its free–free normal vibration modes generated with the interface coordinates loaded with large fictitious masses for obtaining better subsequent coupling results. The normal modes of the j th free–free wing structure (W_j) and those of the body (B), with both substructures loaded at their interface coordinates (I) with large fictitious masses (F), satisfy

$$\begin{bmatrix} K_{W_j W_j} & K_{W_j I_j} \\ K_{W_j I_j}^T & K_{I_j I_j}^{(W_j)} \end{bmatrix} \begin{bmatrix} \phi_{W_j} \\ \phi_{I_j W_j} \end{bmatrix} = \begin{bmatrix} M_{W_j W_j} & M_{W_j I_j} \\ M_{W_j I_j}^T & M_{I_j I_j}^{(W_j)} + M_{F_j}^{(W_j)} \end{bmatrix} \times \begin{bmatrix} \phi_{W_j} \\ \phi_{I_j W_j} \end{bmatrix} [\omega_{W_j}]^2, \quad j = 1 \dots N \quad (2)$$

and

$$[K_B][\phi_B] = [M_{BF}][\phi_B][\omega_B]^2 \quad (3)$$

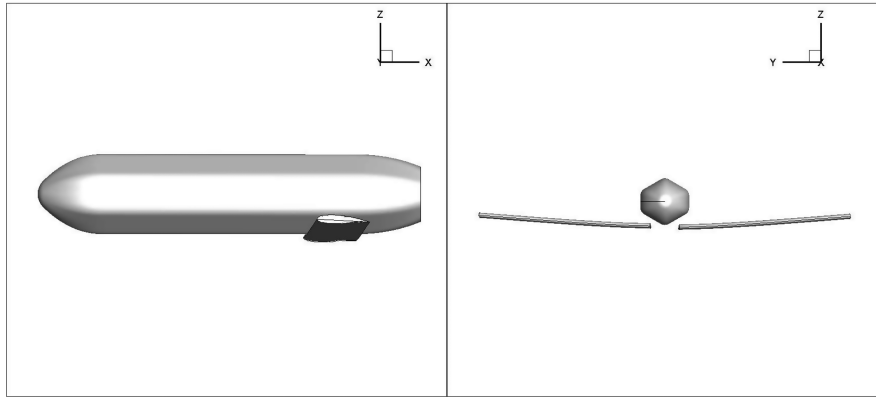


Fig. 2 Example 1 geometry with fully opened wings.

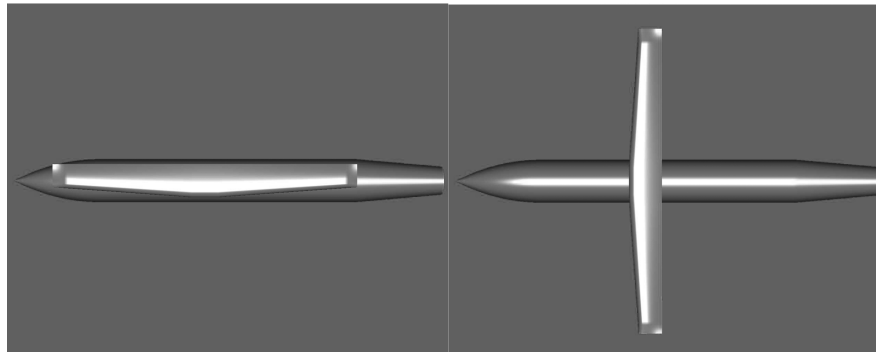


Fig. 3 Example 2 geometry with folded and fully opened wings.

where

$$[K_B] = \begin{bmatrix} K_{BB} & K_{BI_1} & K_{BI_2} & \cdots & K_{BI_N} \\ K_{BI_1}^T & K_{I_1I_1}^{(B)} & 0 & \cdots & 0 \\ K_{BI_2}^T & 0 & K_{I_2I_2}^{(B)} & \cdots & 0 \\ \vdots & \vdots & \vdots & \ddots & \vdots \\ K_{BI_N}^T & 0 & 0 & \cdots & K_{I_NI_N}^{(B)} \end{bmatrix}; \quad [\phi_B] = \begin{bmatrix} \phi_{BB} \\ \phi_{I_1B} \\ \phi_{I_2B} \\ \vdots \\ \phi_{I_NB} \end{bmatrix};$$

$$[M_{BF}] = \begin{bmatrix} M_{BB} & M_{BI_1} & M_{BI_2} & \cdots & M_{BI_N} \\ M_{BI_1}^T & M_{I_1I_1}^{(B)} + M_{F_1}^{(B)} & 0 & \cdots & 0 \\ M_{BI_2}^T & 0 & M_{I_2I_2}^{(B)} + M_{F_2}^{(B)} & \cdots & 0 \\ \vdots & \vdots & \vdots & \ddots & \vdots \\ M_{BI_N}^T & 0 & 0 & \cdots & M_{I_NI_N}^{(B)} + M_{F_N}^{(B)} \end{bmatrix}$$

where $[K]$, $[M]$, and $[\phi]$ are the stiffness, mass, and normal-modes matrices, respectively, and $[\omega]$ is a diagonal matrix of the modal

where $\{u_B\}^T = [u_{BB}^T u_{W_1B}^T \cdots u_{W_NB}^T]$, and $[M_B]$ is equal to $[M_{BF}]$ of Eq. (3) with the fictitious masses removed. Before we add the coupling terms, Eq. (4) is transformed to modal coordinates with the assumption that the displacement vector of each structural component can be expressed as a linear combination of its modes in the frame of reference that floats with it:

$$\begin{Bmatrix} u_B \\ u_{W_1} \\ u_{I_1W_1} \\ \vdots \\ u_{W_N} \\ u_{I_NW_N} \end{Bmatrix} = \begin{bmatrix} \phi_B & 0 & \cdots & 0 \\ 0 & \phi_{W_1} & & \vdots \\ 0 & \phi_{I_1W_1} & & \vdots \\ \vdots & \vdots & \ddots & 0 \\ 0 & 0 & \cdots & \phi_{W_N} \\ 0 & 0 & \cdots & \phi_{I_NW_N} \end{bmatrix} \begin{Bmatrix} \xi_B \\ \xi_{W_1} \\ \vdots \\ \xi_{W_N} \end{Bmatrix} \quad (5)$$

where $\{\xi_B\}$ and $\{\xi_{W_j}\}$ are the component modal displacements. Substitution of Eq. (5) in Eq. (4) and premultiplication by transpose of the modal matrices of Eqs. (2) and (3) yields

$$\begin{bmatrix} M_{ii_B} - \sum_{j=1}^N \phi_{I_jB}^T M_{F_j}^{(B)} \phi_{I_jB} & 0 & \cdots & 0 \\ 0 & M_{ii_{W_1}} - \phi_{I_1W_1}^T M_{F_1}^{(W_1)} \phi_{I_1W_1} & \cdots & 0 \\ \vdots & \vdots & \ddots & \vdots \\ 0 & 0 & \cdots & M_{ii_{W_N}} - \phi_{I_NW_N}^T M_{F_N}^{(W_N)} \phi_{I_NW_N} \end{bmatrix} \begin{Bmatrix} \ddot{\xi}_B \\ \ddot{\xi}_{W_1} \\ \vdots \\ \ddot{\xi}_{W_N} \end{Bmatrix} + \begin{bmatrix} \Omega_B M_{ii_B} & 0 & \cdots & 0 \\ 0 & \Omega_{W_1} M_{ii_{W_1}} & \cdots & 0 \\ \vdots & \vdots & \ddots & \vdots \\ 0 & 0 & \cdots & \Omega_{W_N} M_{ii_{W_N}} \end{bmatrix} \begin{Bmatrix} \xi_B \\ \xi_{W_1} \\ \vdots \\ \xi_{W_N} \end{Bmatrix} = \{0\} \quad (6)$$

frequencies taken into account. Equations (1) and (2) form eigenvalue problems that are solved for the modes and frequencies by finite-element codes such as MSC/NASTRAN. The resulting natural frequencies of each wing component include six zeros that are associated with the rigid-body modes. Because the fictitious masses are large, the elastic modes are close to those of the clamped component.

The discrete-coordinate free undamped equation of motion of the assembled structure, with the structural components still disconnected, is

$$\begin{bmatrix} [M_B] & 0 & \cdots & 0 \\ 0 & M_{W_1W_1} & M_{W_1I_1} & \cdots & 0 \\ 0 & M_{W_1I_1}^T & M_{I_1I_1}^{(W_1)} & \cdots & 0 \\ \vdots & \vdots & \vdots & \ddots & \vdots \\ 0 & 0 & \cdots & M_{W_NW_N} & M_{W_NI_N} \\ & & & M_{W_NI_N}^T & M_{I_NI_N}^{(W_N)} \end{bmatrix} \begin{Bmatrix} \ddot{u}_B \\ \ddot{u}_{W_1} \\ \ddot{u}_{I_1W_1} \\ \vdots \\ \ddot{u}_{W_N} \\ \ddot{u}_{I_NW_N} \end{Bmatrix} + \begin{bmatrix} K_B & 0 & \cdots & 0 \\ 0 & K_{W_1W_1} & K_{W_1I_1} & \cdots & 0 \\ 0 & K_{W_1I_1}^T & K_{I_1I_1}^{(W_1)} & \cdots & 0 \\ \vdots & \vdots & \vdots & \ddots & \vdots \\ 0 & 0 & \cdots & K_{W_NW_N} & K_{W_NI_N} \\ & & & K_{W_NI_N}^T & K_{I_NI_N}^{(W_N)} \end{bmatrix} \begin{Bmatrix} u_B \\ u_{W_1} \\ u_{I_1W_1} \\ \vdots \\ u_{W_N} \\ u_{I_NW_N} \end{Bmatrix} = \{0\} \quad (4)$$

The coupling between the body and the j th wing structural component is introduced by enforcing displacement compatibility at the interface coordinates. The equations depend on the generally nonlinear transformation from the j th wing component coordinate system to the body coordinate system and the time-varying rotation angle ψ_{W_j} that denotes the relative position of the two coordinate systems:

$$\{u_{I_jW_j}\} = [T_{j1}(\psi_{W_j})]\{u_{I_jB}\} + \{T_{j2}\}\psi_{W_j}, \quad j = 1 \dots N \quad (7)$$

where $[T_{j1}]$ and $\{T_{j2}\}$ are particular problem-dependent transformation matrices. For example, the transformation matrices for the model of the second numerical example (next) are

$$[T_1] = \begin{bmatrix} \cos \psi & -\sin \psi & 0 & 0 & 0 & 0 \\ \sin \psi & \cos \psi & 0 & 0 & 0 & 0 \\ 0 & 0 & 1 & 0 & 0 & 0 \\ 0 & 0 & 0 & \cos \psi & -\sin \psi & 0 \\ 0 & 0 & 0 & \sin \psi & \cos \psi & 0 \\ 0 & 0 & 0 & 0 & 0 & 1 \end{bmatrix}; \quad \{T_2\} = \begin{Bmatrix} 0 \\ 0 \\ 0 \\ 0 \\ 0 \\ 1 \end{Bmatrix} \quad (8)$$

The use of Eq. (5) in Eq. (7) yields

$$[\phi_{I_jW_j}]\{\xi_{W_j}\} = [T_{j1}\phi_{I_jB} \quad T_{j2}]\begin{Bmatrix} \xi_B \\ \psi_{W_j} \end{Bmatrix}, \quad j = 1 \dots N \quad (9)$$

Each $\{\xi_{W_j}\}$ may be partitioned into rigid-body and elastic modes $\{\xi_{W_j}^{(R)}\}$ and $\{\xi_{W_j}^{(E)}\}$, respectively, with which constraint equation sets may be written in the form

$$\{\xi_{W_j}^{(R)}\} = [\phi_{I_j W_j}^{(R)}]^{-1} \begin{bmatrix} -\phi_{I_j W_j}^{(E)} & T_{j1} \phi_{I_j B} & T_{j2} \end{bmatrix} \begin{Bmatrix} \xi_{W_j}^{(E)} \\ \xi_B \\ \psi_{W_j} \end{Bmatrix}, \quad j=1 \dots N \quad (10)$$

and a global transformation may be defined by

$$\{\xi\} = [T]\{\xi_1\} \quad (11)$$

where

$$\{\xi\} = \begin{Bmatrix} \xi_B \\ \xi_{W_1} \\ \vdots \\ \xi_{W_N} \end{Bmatrix} = \begin{Bmatrix} \xi_B \\ \xi_{W_1}^{(R)} \\ \xi_{W_1}^{(E)} \\ \vdots \\ \xi_{W_N}^{(R)} \\ \xi_{W_N}^{(E)} \end{Bmatrix}; \quad \{\xi_1\} = \begin{Bmatrix} \xi_B \\ \xi_{W_1}^{(E)} \\ \vdots \\ \xi_{W_N}^{(E)} \\ \psi_1 \\ \vdots \\ \psi_N \end{Bmatrix}$$

$$[T] = \begin{bmatrix} I & 0 & \dots & 0 & 0 & \dots & 0 \\ -[\phi_{I_1 W_1}^{(R)}]^{-1} T_{11} \phi_{I_1 B} & -[\phi_{I_1 W_1}^{(R)}]^{-1} \phi_{I_1 W_1}^{(E)} & \dots & 0 & -[\phi_{I_1 W_1}^{(R)}]^{-1} T_{12} & \dots & 0 \\ 0 & I & \dots & 0 & 0 & \dots & 0 \\ \vdots & \vdots & \ddots & \vdots & \vdots & \ddots & \vdots \\ -[\phi_{I_N W_N}^{(R)}]^{-1} T_{N1} \phi_{I_N B} & 0 & \dots & -[\phi_{I_N W_N}^{(R)}]^{-1} \phi_{I_N W_N}^{(E)} & 0 & \dots & -[\phi_{I_N W_N}^{(R)}]^{-1} T_{N2} \\ 0 & 0 & \dots & I & 0 & \dots & 0 \end{bmatrix}$$

The size of $\{\xi_1\}$ and $[T]$ may be reduced by assuming additional geometry constraints such as the same rotation angle history $\psi(t)$ for a number of wing structural components (as will be shown in the numerical example), which means that one actuator is applied to several structural components.

The differentiation of Eq. (11) with respect to time yields

$$\dot{\{\xi\}} = [T]\dot{\{\xi_1\}} + [\dot{T}]\{\xi_1\}; \quad \ddot{\{\xi\}} = [T]\ddot{\{\xi_1\}} + 2[\dot{T}]\dot{\{\xi_1\}} + [\ddot{T}]\{\xi_1\} \quad (12)$$

The only time-dependent terms in $[T]$ are the $[T_{j1}]$ terms due to the dependency of ψ_j on time. For constructing the forced equation of motion, we assume in this work that the actuation force on each wing component is an internal elastic moment due to a preloaded rotational spring connecting the wing to the body at the interface. The substitution of Eqs. (11) and (12) in Eq. (6), the addition of a modal damping matrix, and the premultiplication by $[T]^T$ yield the nonlinear free equation of motion. A vector of generalized forces is then added based on the aerodynamic forces and the inertial forces due to the rotation of the local wing coordinate systems relative to that of the body, which yields

$$[M_{ii}]\ddot{\{\xi_1\}} + [C_{ii}]\dot{\{\xi_1\}} + [K_{ii}]\{\xi_1\} = [T]^T \begin{Bmatrix} \bar{\phi}_B^T F_B \\ \bar{\phi}_{W_1}^T F_{W_1} \\ \vdots \\ \bar{\phi}_{W_N}^T F_{W_N} \\ 0 \\ \vdots \\ 0 \end{Bmatrix} \quad (13)$$

where $\{F_B\}$, $\{F_{W_1}\}$, \dots , $\{F_{W_N}\}$ are the forces applied to the body and wing components in the respective coordinate systems, and $\{\bar{\phi}_B\}$, $\{\bar{\phi}_{W_1}\}$, \dots , $\{\bar{\phi}_{W_N}\}$ are the respective modal displacements at the locations of force application. A detailed description of the forces that are applied to each rotating wing component is presented next.

The generalized matrices on the left side of Eq. (13) are

$$\begin{aligned} [M_{ii}] &= [T]^T [M_{ii}] [T] \\ [C_{ii}] &= [T]^T ([C_{ii}] [T] + 2[M_{ii}] [\dot{T}]) \\ [K_{ii}] &= [T]^T ([K_{ii}] [T] + [C_{ii}] [\dot{T}] + [M_{ii}] [\ddot{T}]) \end{aligned} \quad (14)$$

where $[M_{ii}]$ and $[K_{ii}]$ are the mass and stiffness matrices of Eq. (6), and $[C_{ii}]$ is a modal-damping matrix usually taken as a diagonal

matrix. Equation (13) can be converted to the time-variant nonlinear state-space form:

$$\begin{Bmatrix} \dot{\xi_1} \\ \xi_1 \end{Bmatrix} = \begin{bmatrix} 0 & I \\ -M_{ii}^{-1} C_{ii} & -M_{ii}^{-1} K_{ii} \end{bmatrix} \begin{Bmatrix} \xi_1 \\ \xi_1 \end{Bmatrix} + \begin{bmatrix} 0 \\ -M_{ii}^{-1} T^T \end{bmatrix} \begin{Bmatrix} \bar{\phi}_B^T F_B \\ \bar{\phi}_{W_1}^T F_{W_1} \\ \vdots \\ \bar{\phi}_{W_N}^T F_{W_N} \\ 0 \\ \vdots \\ 0 \end{Bmatrix} \quad (15)$$

and solved using time-marching schemes such as the Runge–Kutta or Adams–Bashforth methods [36].

IV. Applied Forces

The forces that appear in the right-hand side of Eq. (15) are the aerodynamic forces and the inertial forces due to rotational motion of the wings relative to the body. The aerodynamic forces that act on the surface of the flight vehicle are extracted from the CFD solution after the completion of each step and are transformed to the generalized coordinates using Eq. (1). The modal displacements in the aerodynamic grid required for the transformation should be prepared before the simulation starts.

The modal equations of motion were developed under the assumptions of small displacements and linearity. The compatibility

equation (7) transforms the wing displacements to the body coordinate system but does not take into account the relative angular velocity and acceleration in a full manner. Hence, when relative angular motion occurs, each mass point on the wing experiences additional acceleration terms that yields inertial forces. This should be added to the aerodynamic forces. The relative-rotation induced force on a mass point m is

$$f_{\Omega} = -m \frac{d\Omega}{dt} \times \mathbf{r} - 2m\Omega \times \frac{d\mathbf{r}}{dt} - m\Omega \times (\Omega \times \mathbf{r}) \quad (16)$$

where Ω is the relative angular velocity vector, and \mathbf{r} is the location of the mass element relative to a reference point at the wing-body interface in the rotating system. The three terms in the right-hand side of Eq. (16) are the Euler, Coriolis, and centrifugal forces, respectively. The Euler force is already included in Eq. (15). The influence of the Coriolis force is often negligible. In the current work, the effect of the Coriolis force has been investigated at the early stages of the research and subsequently neglected.

The deformed grid-point locations of the j th wing component (W_j) in the local coordinate system can be written as

$$\{r_{W_j}\} = \{r_{0,W_j}\} + \{u_{W_j}\} \quad (17)$$

where $\{r_{0,W_j}\}$ is the vector of undeformed locations, and $\{u_{W_j}\}$ is extracted from the component elastic modes. The last term in Eq. (16), with the deformed locations of Eq. (17), is used to calculate centrifugal forces on the mass elements. Before being used for calculating the inertial part of the generalized forces in Eq. (15), each centrifugal forces vector should be rotated to a local coordinate system that rotates with the respective point, which yields

$$\mathbf{f}_{\Omega_1} = \mathbf{f}_{\Omega} - \boldsymbol{\theta} \times \mathbf{f}_{\Omega} \quad (18)$$

where $\boldsymbol{\theta}$ is the vector of grid orientation angles relative to the component coordinate system. Equation (18) is consistent with the small-displacement assumption associated with the elastic deformations. When applied to a rotating wing about a perpendicular axis, Eq. (18) represents the out-of-plane stiffening effect of the rotation rate.

To calculate the inertial forces using Eqs. (17) and (18), the whole finite-element structural model of the wing is required. Detailed structural models may have thousands of nodes, which may substantially increase computation time. In such cases, it is desirable to simplify the finite-element model.

V. Numerical Examples

A. Morphing Vehicle Models

The application of the method described previously is illustrated with two sample cases of body-wing configurations. The first configuration (example 1) consists of a slender body fuselage that has a hexagonal cross section and a pair of wings, which are adjusted tightly to the fuselage sides in the folded position of Fig. 1 and are opened to the vertical position of Fig. 2. The rotation angle of each wing is -93.75° at the beginning of the morphing process and 0° at the end of the process. The rotation is driven by a preloaded spring whose nominal constant is $K_{act} = 200 \text{ N} \cdot \text{m/deg}$ and unstrained position at $\psi = 0^\circ$. When reaching $\psi = 0^\circ$, a large spring of $K = 100 \cdot K_{act}$ is added to simulate the locking mechanism. Also, a damping term of $0.1 \cdot \sqrt{I_{zz}} \cdot K_{act}$, where I_{zz} is the wing moment of inertia in yaw, was added at this point to $[C_{ii}]$ to suppress post-lock vibrations. The structure was represented in the equations of motion of example 1 by 17 free-free modes of each wing, up to a frequency of 1065 Hz, and 20 clamped modes of the body, up to a frequency of 975 Hz, that were calculated separately, such that the total number of component modes was 54. The modes of the body and the wings were calculated with the interfaces loaded by fictitious masses of 100 kg and fictitious moments of inertia of $10 \text{ kg} \cdot \text{m}^2$. With 10 rigid-body modes (five for each wing) eliminated by the displacement constraints of Eq. (10), the total number of degrees of freedom becomes 44. Some simplifications

were made in the original aerodynamic configuration to speed up the CFD solution. The gaps between the fuselage and the wings in the folded position were slightly increased; the rods connecting the wings to the fuselage were omitted; and the rotation angles were forced to be the same for the right and left wings at every time step. These changes allow a significant reduction of the number of grid points in the CFD mesh with no significant effects on the solution. The CFD grid used for example 1 consists of five zones and has about 2.9 million grid points. The maximal grid resolution is 0.3 mm around the body and 0.04 mm around the wings.

The second configuration (example 2) consists of a slender body having a circular cross section with a rotating wing adjusted tightly to the top of the fuselage. The motion starts when the wing is parallel to the body ($\psi = -90^\circ$) and ends when the wing is fully opened ($\psi = 0^\circ$), as shown in Fig. 3. The motion-driving mechanism is the same as for example 1. Twenty-eight modes of the wing and six of the fuselage, up to a frequency of 325 Hz, were taken into account in the derivation of the structural equations. The modes were calculated using the same fictitious masses as in example 1 and fictitious moments of inertia of $100 \text{ kg} \cdot \text{m}^2$. The CFD grid used for example 2 consists of two zones and has about 1 million grid points. The maximal grid resolution around the surface is about 0.3 mm.

Numerical simulations of the inviscid flow about the morphing configurations described previously were conducted. The solutions were first converged about the folded rigid configurations and then continued with added actuator springs, which caused the wings to rotate about their axes. The flow conditions for example 1 are sea-level altitude, freestream Mach number of $M_\infty = 0.3$, and a number of angles of attacks ranging from 0 to 10° . The flow conditions for example 2 are sea-level altitude, freestream Mach number of $M_\infty = 0.7$, and an angle of attack of 5.7° . For example 2, the influence of the structural stiffness on the deployment process was investigated by multiplying the modal stiffness matrices of all the substructures by a coefficient called the flexibility factor.

Both simulations were conducted using the AUSM⁺-up CFD numerical scheme [26–28] with the limiter [30] turned on, with a dimensionless time step of 0.1, which corresponds to a physical time step of about $3 \cdot 10^{-4} \text{ s}$, and 10 subiterations. The structural equations of motion were advanced with 20 substeps to assure numerical stability.

B. Verification of the Modal-Coupling Process

The modal coupling process was verified by comparing the natural frequencies at several positions along the morphing path, calculated from the modal-coupling equations, with the ones calculated directly from the finite-element model. The modal-coupling frequencies were calculated by eigenvalue analysis of Eq. (13) with the damping and forcing terms ignored and with the generalized mass and stiffness matrices of Eq. (14) with $[\dot{T}] = [\ddot{T}] = 0$. The resulting natural frequencies and eigenvectors satisfy

$$[T]^T [K_{ii}] [T] [\Psi_1] = [T]^T [M_{ii}] [T] [\Psi_1] [\omega_1]^2 \quad (19)$$

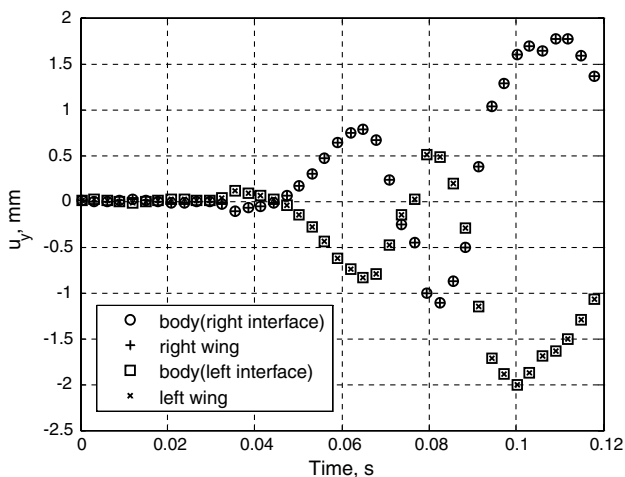
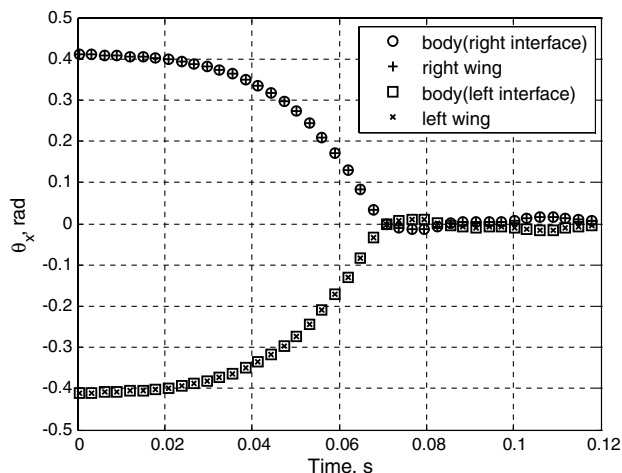
where $[\Psi_1]$ is the matrix of eigenvectors in generalized coordinates, $[\omega_1]$ is a diagonal matrix of the respective natural frequencies, and $[T]$ is a function of the opening angle ψ , as in Eq. (7). A sample comparison is given in Table 1 for example 1 at $\psi = -60^\circ$ for each wing. With 24 large fictitious inertia terms and 10 eliminated rigid-body modes, the first 30 modes ($44 + 10 - 24$) should be of good accuracy. Indeed, Table 1 shows excellent accuracy of the coupling process for the first 30 frequencies. The higher coupling frequencies do not reflect actual natural modes but represent the local near-boundary deformations necessary for accurate modal coupling, as demonstrated by the accuracy of all the natural frequencies up to 1000 Hz in all the cases. The comparison of modal shapes also shows a good agreement between two calculation methods.

The dynamic coupling process was validated by checking that the interface displacements and rotations satisfy the compatibility equations (7) along the morphing process. Figures 4 and 5 show the side displacements and roll angles, calculated at the wing and body interface for example 1 at $\alpha = 5^\circ$ and $\beta = 10^\circ$. The

Table 1 Comparison of the frequencies for $\psi = -60$ deg

| Mode number | NASTRAN, Hz | Modal decomposition, Hz | Coupling error, % |
|-------------|-------------|-------------------------|-------------------|
| 1 | 3.727 | 3.727 | 0.00 |
| 2 | 3.727 | 3.727 | 0.00 |
| 3 | 21.364 | 21.371 | 0.03 |
| 4 | 21.444 | 21.452 | 0.04 |
| 5 | 32.692 | 32.692 | 0.00 |
| 6 | 36.367 | 36.367 | 0.00 |
| 7 | 128.759 | 128.798 | 0.03 |
| ... | | | |
| 25 | 793.430 | 795.824 | 0.30 |
| 26 | 863.292 | 866.297 | 0.35 |
| 27 | 869.537 | 874.654 | 0.59 |
| 28 | 892.604 | 894.777 | 0.24 |
| 29 | 1049.06 | 1060.91 | 1.13 |
| 30 | 1050.71 | 1062.67 | 1.14 |
| 31 | 1117.19 | 1458.59 | 30.56 |
| 32 | 1118.86 | 1613.83 | 44.24 |
| ... | | | |
| 44 | 1649.12 | 29135.28 | 1667 |

body interface displacements and rotations are transformed to the respective wing coordinate systems. The results show full interface displacement compatibility. Similar consistency exists for all the displacement components at each solution.

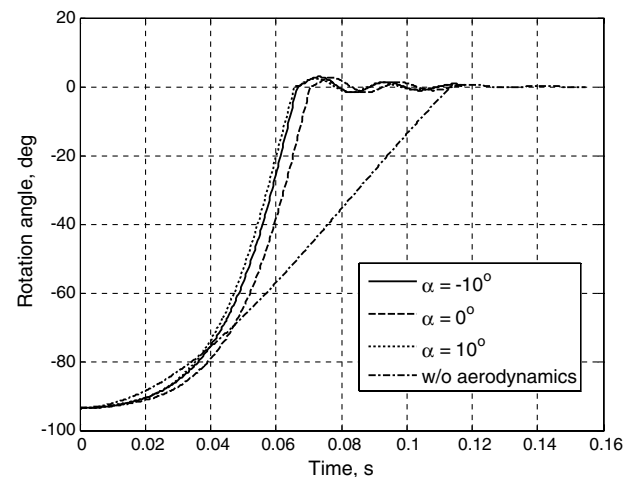
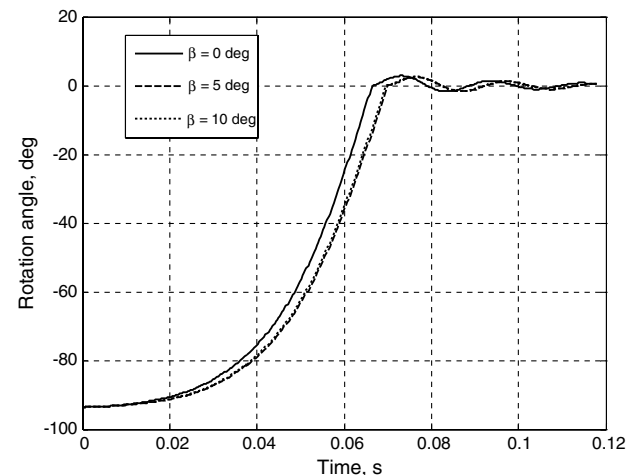
**Fig. 4** Side displacement compatibility at wing-body interface (example 1).**Fig. 5** Roll rotation compatibility at wing-body interface (example 1).

C. Time History of Wing Rotation Angle

Figures 6–8 show the time histories of the rotation angle as functions of various incidence angles and actuator stiffness constants for example 1. The solution of the structural equations of the motion without aerodynamic force application is also presented in Fig. 6. As can be seen, the aerodynamic forces slow down the deploying process at the beginning of the motion, but then the process is accelerated such that the deploying time with the presence of aerodynamic forces is almost half of that without aerodynamics. The slow-down at the beginning is the result of suction that occurs between the wing and the body. The angle of attack and the slip-stream angle (see Fig. 7) have small effect on the rotation. This is an expected result because, during most of the deployment time, the wings have significant negative incidence relative to the air stream, and the variations of the angle of attack are much smaller than the geometric inclination angle of the wings. The influence of the actuator spring constant on the rotating angle time history, Fig. 8, is mostly at the initial stage of morphing process. As the influence of aerodynamic forces increases with the rotation angle, the influence of the actuator spring vanishes. The time history of the rotation angle in example 2 is shown in Fig. 9 with the effects of the structure flexibility factor. It shows that the factor has a negligible effect on the rotation angle.

D. Structural Displacements

Figures 10–12 demonstrate the influence of aerodynamic forces on the structural deformations for example 1. Figures 10 and 11 show the wing-tip displacements and pitch angle calculated from the

**Fig. 6** Time history of wing rotation angle for various angles of attack (example 1).**Fig. 7** Time history of wing rotation angle for various side-slip angles (example 1).

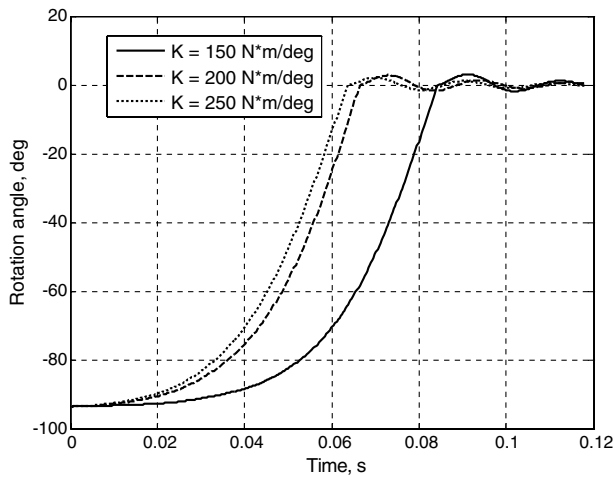


Fig. 8 Time history of wing rotation angle for various actuator spring constants (example 1).

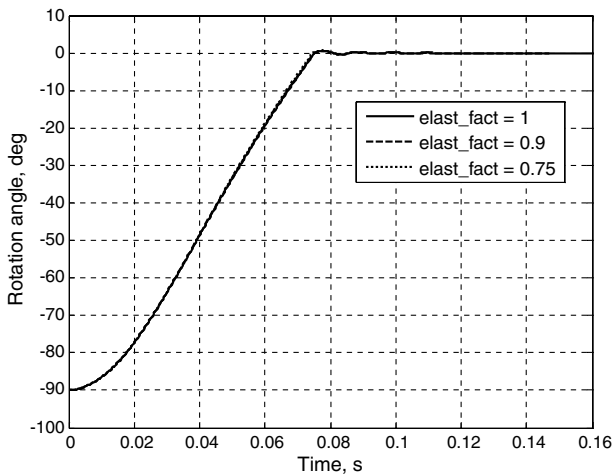


Fig. 9 Time history of wing rotation angle for various flexibility factors (example 2).

solution of the structural equations of motion without aerodynamics. Figure 12 shows the out-of-plane displacements with the CFD aerodynamic forces included for various angles of attack. The associated chordwise (in the x direction of the local wing system) and longitudinal (stretching) displacements (not shown) are much smaller. All the displacements are shown in the wing coordinate

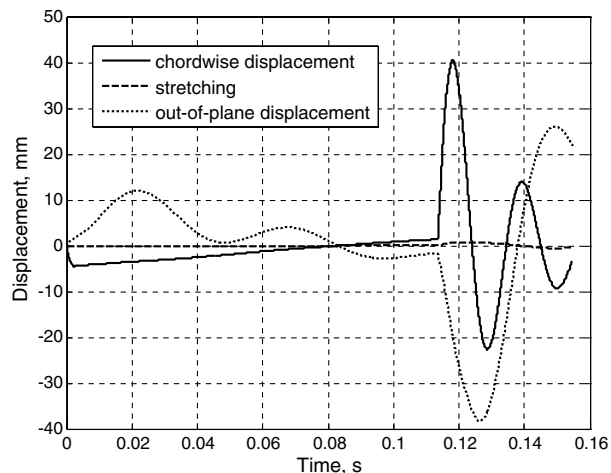


Fig. 10 Wing-tip structural displacements in absence of aerodynamic loads (example 1).

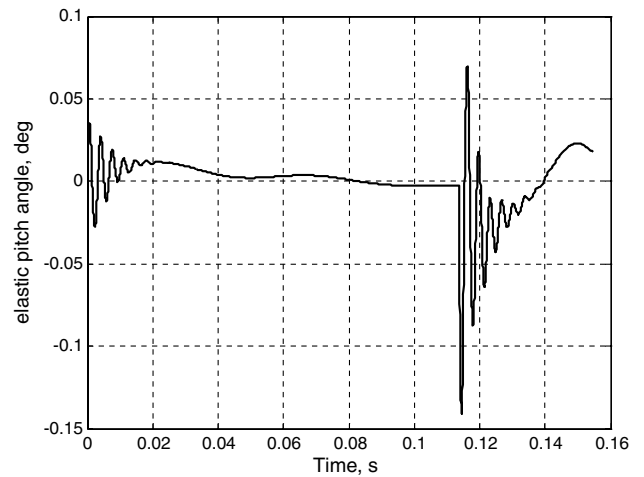


Fig. 11 Wing-tip elastic pitch angle in absence of aerodynamic loads (example 1).

system. As can be seen, the aerodynamic loads affect the structural displacements significantly, with the out-of-plane displacements increased by an order of magnitude, and the elastic pitch angle changes its behavior pattern. As expected, the amplitude of the out-of-plane displacement increases with the aerodynamic loads, but the elastic pitch angle of Fig. 13 does not follow the same pattern.

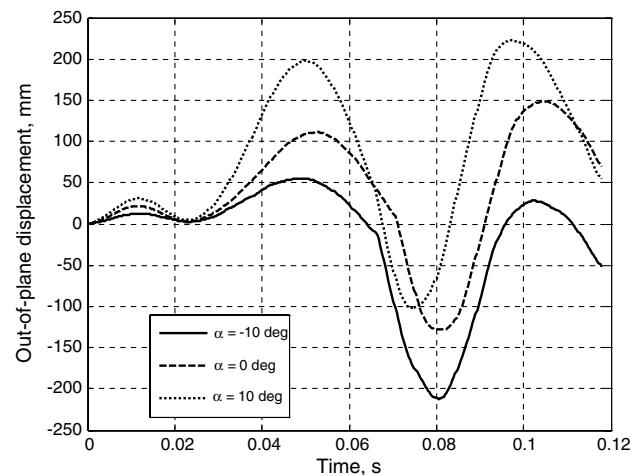


Fig. 12 Wing-tip structural displacements in the full CFD solution (example 1).

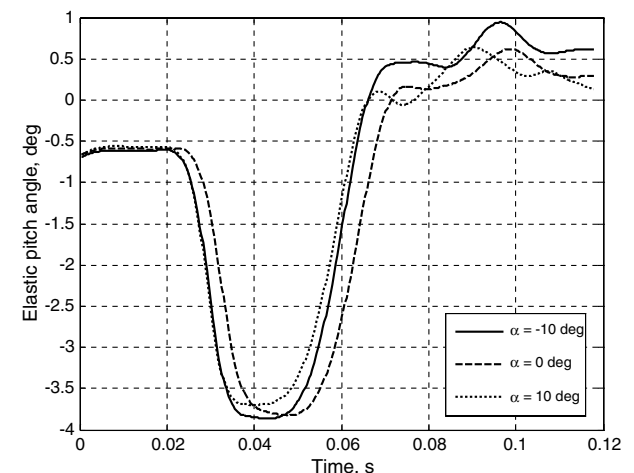


Fig. 13 Wing-tip elastic pitch angle in the full CFD solution (example 1).

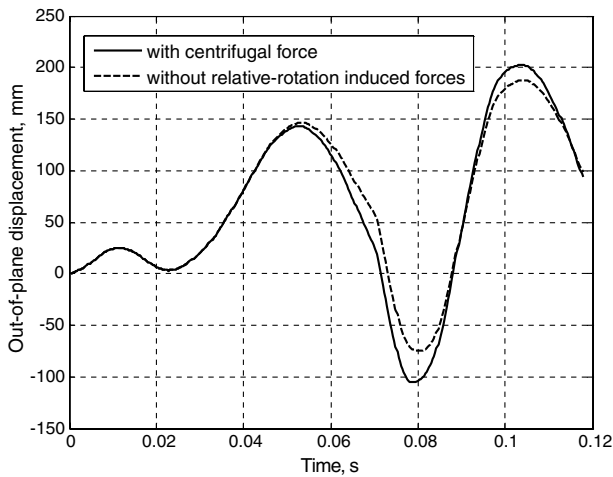


Fig. 14 Influence of the centrifugal forces on the out-of-plane displacements (example 1).

Figure 14 shows the influence of centrifugal forces on the out-of-plane displacements of example 1. The centrifugal forces stiffen the wing and decrease the maximal out-of-plane deflection by approximately 10%. Figure 15 shows the influence of side-slip angle on the out-of-plane deflection for example 1. The deflections are shown for both tips of the wing. As can be seen, the right and left out-of-plane displacements differ mostly at the final stage of the morphing and during the post-lock vibrations. The right wing deflections are greater in magnitude because the left wing is partially hidden. Figure 16 indicates that the influence of the spring constant on the out-of-plane bending deformations, shown versus wing rotation angle, is small. The influences of Figs. 14–16 are shown for the case of a 5 deg angle of attack. In all these cases, the wing-tip elastic pitch angle is not influenced significantly.

Figures 17–19 show the wing-tip displacements and elastic pitch angle of example 2. All displacements are shown in relative to the wing coordinate system. Unlike for example 1, the out-of-plane and chordwise displacements are of similar magnitudes in this case. The motions before and after the wing hits the stop at fully deployed position are of different nature. Before hitting the stop, the deformations are mainly a direct result of the current aerodynamic loads (described next) and are almost symmetric with small to moderate antisymmetric deviations. The deformations after hitting the stop are mainly antisymmetric at high frequencies (about 100 Hz) due to the stop impact. The torsion deformations at the right wing tip are shown in Fig. 19 for the nominal and the reduced stiffness cases. We can see that the deformation increases are generally proportional to the inverse of the applied flexibility factors, as expected.

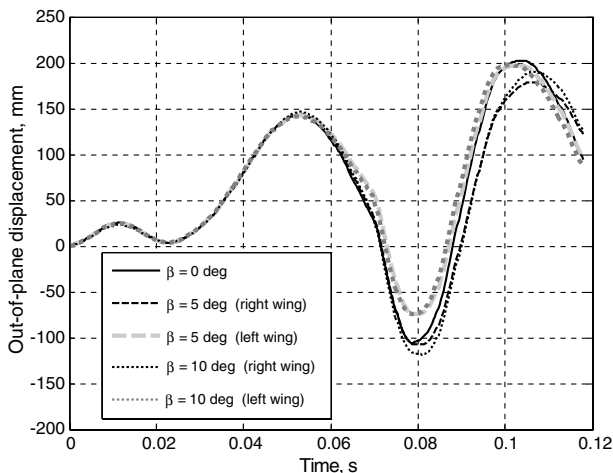


Fig. 15 Influence of side-slip angle on the out-of-plane displacements (example 1).

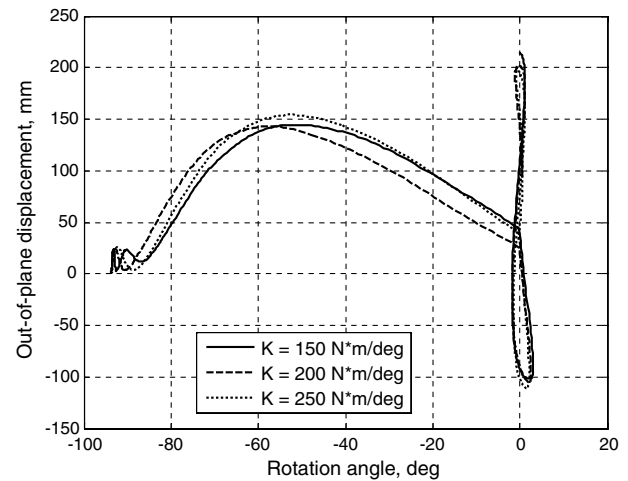


Fig. 16 Actuator spring influence on the structural displacements (example 1).

E. Aerodynamic Forces and Moments

The aerodynamic forces defined in this section are relative to the body longitudinal axis. The reference area is the area of the fully deployed wing. Figures 20 and 21 show the time history of the lift force for examples 1 and 2 as a function of the wing relative-rotation angle. As can be seen, the lift force gradually increases as the wings are deployed. For example 1, while the dependency of the lift coefficient on the deployment angle is close to linear at positive

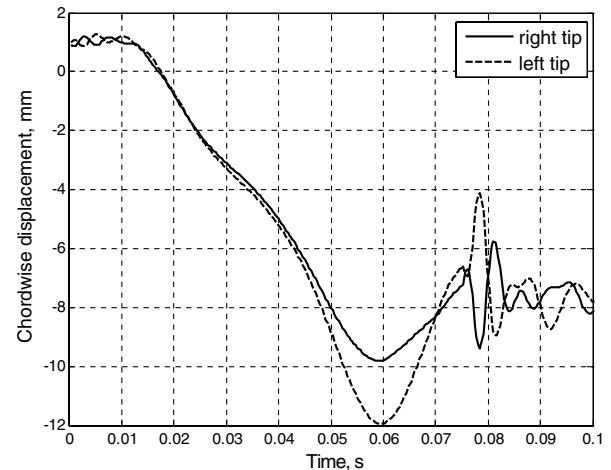


Fig. 17 Chordwise wing-tip displacements (example 2).

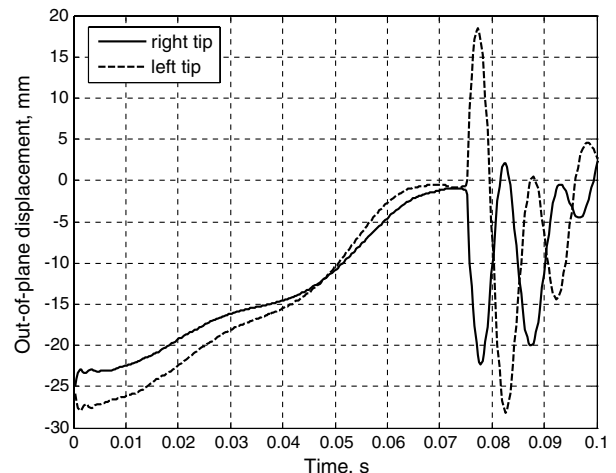


Fig. 18 Out-of-plane wing-tip displacements (example 2).

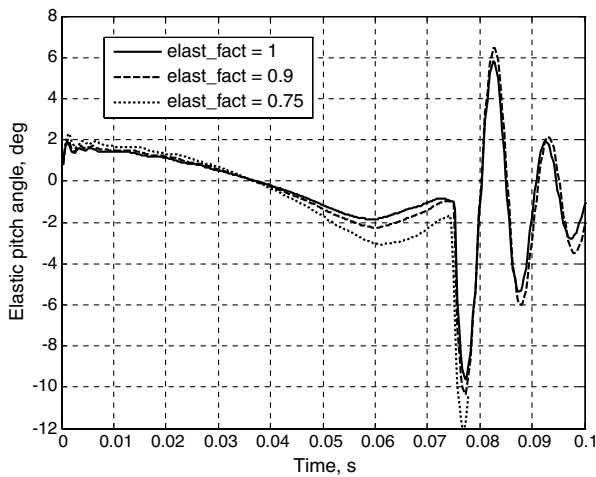


Fig. 19 Wing-tip elastic pitch angle for various flexibility factors (example 2).

angles of attack, it is more complex for the negative angles. The time history of the drag coefficient for example 1 is shown in Fig. 22. As can be seen, for all angles of attack, the drag coefficient remains approximately constant during the deployment and it has approximately the same value. This indicates that the induced drag component is negligible during the deployment process. For example 2, the drag coefficient shown in Fig. 23 grows monotonously with the wing opening angle.

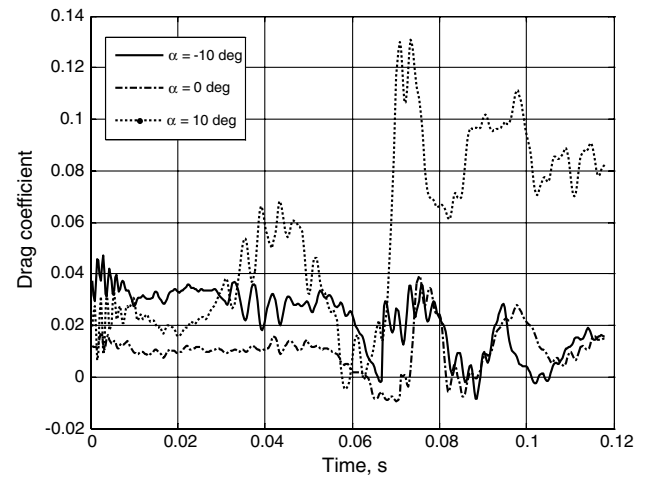


Fig. 22 Transient drag coefficient vs time (example 1).

Figure 24 shows the time history of the pitching moment coefficient for example 1. The backward movement of the center of pressure as the wings deploy is clearly seen. The aerodynamic moment coefficients of example 2 are shown in Figs. 25–27. They change more rapidly and exhibit vibrations, sign changes, and significant aeroelastic effects. The rolling moment (Fig. 25) starts negative due to the higher aerodynamic efficiency of the left wing at small opening angles even though aeroelastic effects reduce its effectiveness, as can be deduced from the differences between the curves of the nominal and the reduced stiffness. At larger angles, the

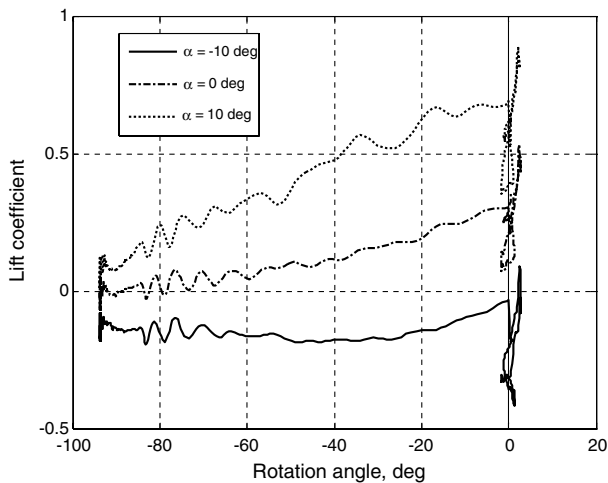


Fig. 20 Transient lift coefficient vs rotation angle (example 1).

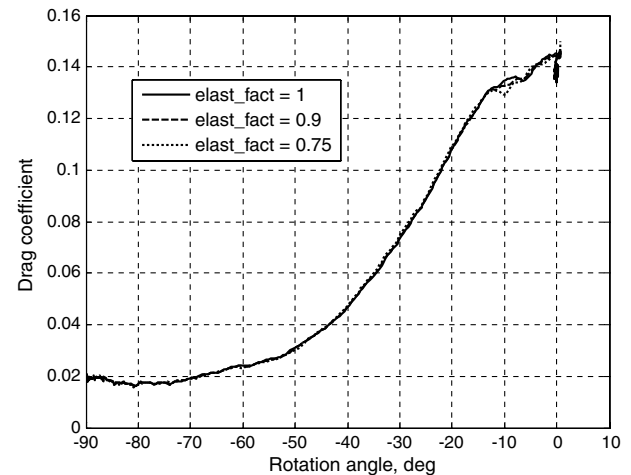


Fig. 23 Transient drag coefficient vs rotation angle (example 2).

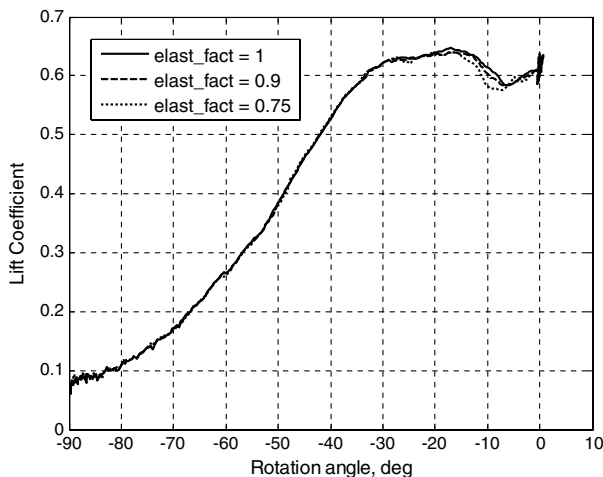


Fig. 21 Transient lift coefficient vs rotation angle (example 2).

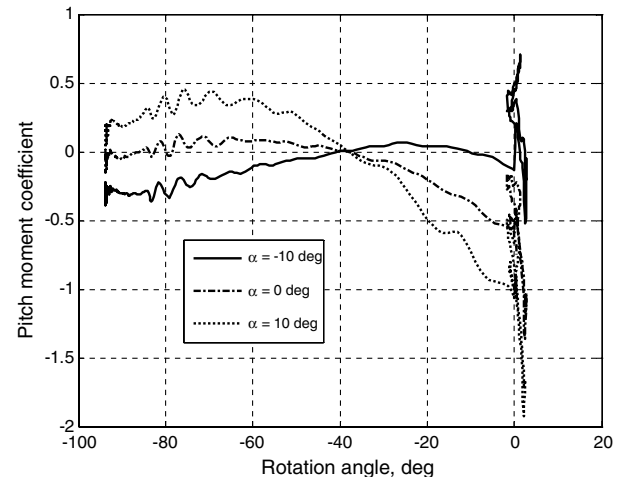


Fig. 24 Pitch moment coefficient of example 1.

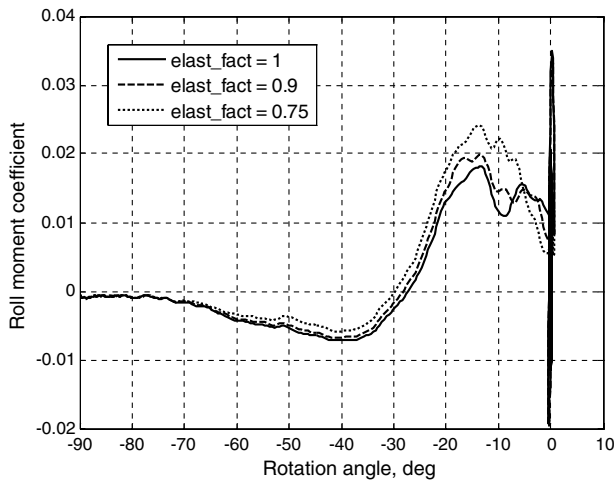


Fig. 25 Roll moment coefficient of example 2.

right wing becomes more effective, both aerodynamically and aeroelastically, which rolls the vehicle to the left. The pitching moment (Fig. 26) starts with large nose-up values, magnified by aeroelastic effects due to the right wing being swept forward, reduces when the left wing becomes more dominant, and increases again at low ψ values before settling to a small steady value after the wing hits the stop. The yawing moment (Fig. 27) is larger at high opening angles due to larger drag on the right wing, induced by the larger lift on it, as implied by the positive rolling moment (see Fig. 25).

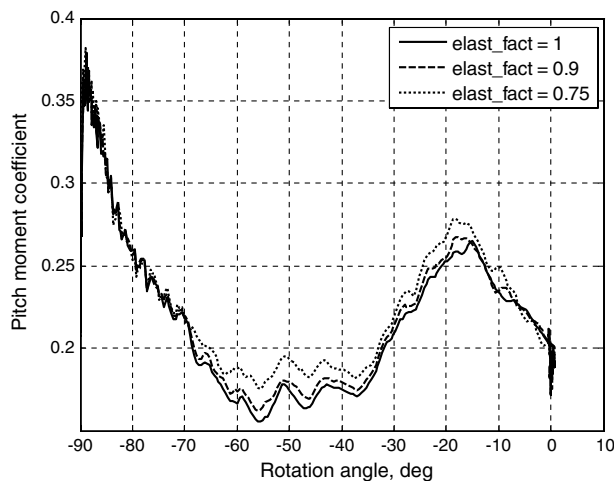


Fig. 26 Pitch moment coefficient of example 2.

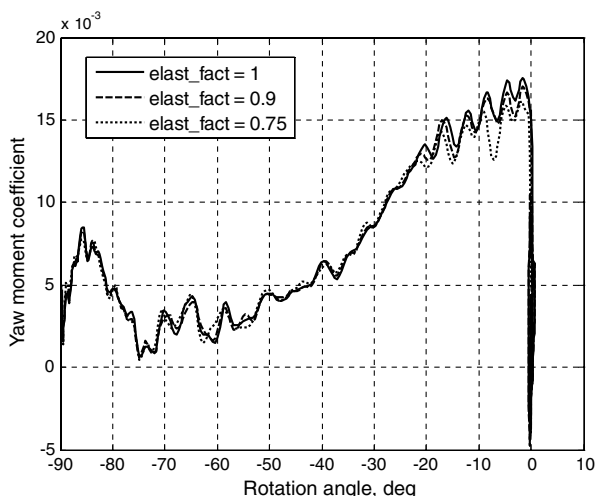


Fig. 27 Yaw moment coefficient of example 2.

VI. Conclusions

An efficient method for high-fidelity simulations of morphing flight vehicles was presented in this work. The method allows obtaining the dynamic equations of motion of the interconnected structures with any degree of complexity by using the fictitious-mass modal coupling method, which was extended to handle large rotations between the structures by adding compatibility equations. The compatibility equations are time-dependent, and the inclusion of their time derivatives in the equations of motion brings into account the nonlinear time-dependent dynamic effects. The account for nonlinear inertial effects of rotating structures allows obtaining a full picture of the transient nonlinear aeroelastic response and the aerodynamic loads during the rapid morphing process based on linear normal modes of the substructures. The method was applied to numerical examples with clamped body. Extension to cases of free body would require the addition of flight-mechanics terms that deal with the rotating coordinate system. The application to two different morphing vehicle structures at various flight conditions illustrates the method robustness. Both numerical examples demonstrated stable computational processes. The presented numerical examples show that the transient elastic deformations and aerodynamic loads may have significant influence on the vehicle stability and control characteristics.

References

- [1] Wilson, J. R., "Morphing UAVs Change the Shape of Warfare," *Aerospace America*, Vol. 42, Part 2, Feb. 2004, pp. 28–29.
- [2] Reich, G. W., Bowman, J. C., Sanders, B., and Frank, G. J., "Development of an Integrated Multibody Morphing Simulation Tool," *47th AIAA/ASME/ASCE/AHS/ASC Structures, Structural Dynamics, and Materials Conference*, Newport, RI, AIAA Paper 2006-1892, May 2006.
- [3] Scarlett, J. N., Canfield, R. N., and Sanders, B., "Multibody Dynamic Aeroelastic Simulation of a Folding Wing Aircraft," *47th AIAA/ASME/ASCE/AHS/ASC Structures, Structural Dynamics, and Materials Conference*, Newport, RI, AIAA Paper 2006-2135, May 2006.
- [4] Craig, R. R., and Bampton, M. C. C., "Coupling of Substructures for Dynamic Analyses," *AIAA Journal*, Vol. 6, No. 7, July 1968, pp. 1313–1319. doi:10.2514/3.4741
- [5] Ameri, N., Lowenberg, M. H., and Friswell, M. I., "Modelling the Dynamic Response of a Morphing Wing with Active Winglets," *AIAA Atmospheric Flight Mechanics Conference and Exhibit*, Hilton Head, SC, AIAA Paper 2007-6500, Aug. 2007.
- [6] Obradovic, B., and Subbarao, K., "Modeling and Simulation to Study Flight Dynamics of a Morphable Wing Aircraft," *AIAA Modeling and Simulation Technologies Conference*, Chicago, AIAA Paper 2009-6240, Aug. 2009.
- [7] Liu, D. D., Chen, P. C., Zhang, Z., Wang, Z., Yang, S., Lee, D. H., et al., "Continuous Dynamic Simulation for Morphing Wing Aeroelasticity," *50th AIAA/ASME/ASCE/AHS/ASC Structures, Structural Dynamics, and Materials Conference*, Palm Springs, CA, AIAA Paper 2009-2572, May 2009.
- [8] Seigler, T. M., Neal, D. A., Bae, J., and Inman, D. J., "Modeling and Flight Control of Large-Scale Morphing Aircraft," *Journal of Aircraft*, Vol. 44, No. 4, July–Aug. 2007, pp. 1077–1087. doi:10.2514/1.21439
- [9] Tang, D., and Dowell, E. H., "Theoretical and Experimental Aeroelastic Study for Folding Wing Structures," *Journal of Aircraft*, Vol. 45, No. 4, July–Aug. 2008, pp. 1136–1147. doi:10.2514/1.32754
- [10] Geradin, M., and Cardona, A., *Flexible Multibody Dynamics, A Finite Element Approach*, Wiley, West Sussex, England, U.K., 2001; Chap. 8.
- [11] Rubin, S., "Improved Component-Mode Representation for Structural Dynamic Analysis," *AIAA Journal*, Vol. 13, No. 8, Aug. 1975, pp. 995–1006. doi:10.2514/3.60497
- [12] Karpel, M., and Newman, M., "Accelerated Convergence for Vibration Modes Using the Substructure Coupling Method and Fictitious Masses," *Israel Journal of Technology*, Vol. 13, May 1975, pp. 55–62.
- [13] Karpel, M., and Raveh, D. E., "Fictitious Mass Element in Structural Dynamics," *AIAA Journal*, Vol. 34, No. 3, 1996, pp. 607–613. doi:10.2514/3.13111
- [14] Bhardwaj, M. K., Kapania, R. K., Reichenbach, E., and Guruswamy,

- G. P., "Computational Fluid Dynamics/Computational Structural Dynamics Interaction Methodology for Aircraft Wings," *AIAA Journal*, Vol. 36, No. 12, Dec. 1998, pp. 2179–2186.
doi:10.2514/2.342
- [15] Raveh, D., "Computational-Fluid-Dynamics-Based Aeroelastic Analysis and Structural Design Optimization—A Researcher's Perspective," *Computer Methods in Applied Mechanics and Engineering*, Vol. 194, 2005, pp. 3453–3471.
doi:10.1016/j.cma.2004.12.027
- [16] Alonso, J., and Jameson, A., "Fully-Implicit Time-Marching Aeroelastic Solutions," *AIAA Aerospace Sciences Meeting and Exhibit*, Reno, NV, AIAA Paper 1994-0056, Jan. 1994.
- [17] Demasi, L., and Livne, E., "Aeroelastic Coupling of Geometrically Nonlinear Structures and Linear Unsteady Aerodynamics: Two Formulations," *Journal of Fluids and Structures*, Vol. 25, No. 5, July 2009, pp. 918–935.
doi:10.1016/j.jfluidstructs.2009.03.001
- [18] Farhat, C., "CFD-Based Nonlinear Computational Aeroelasticity," *Encyclopedia of Computational Mechanics*, edited by E. Stein, R. de Borst and T. J. R. Hughes, Vol. 3, Wiley, West Sussex, England, U.K., 2004, Chap. 13.
- [19] Karpel, M., Yaniv, S., and Livshits, D. S., "Integrated Solution for Computational Static Aeroelastic Problems," *Journal of Spacecraft and Rockets*, Vol. 35, No. 5, 1998, pp. 612–618.
doi:10.2514/2.3393; also AIAA Paper 1996-4012, 1996.
- [20] Raveh, D. E., Karpel, M., and Yaniv, S., "Nonlinear Design Loads for maneuvering Elastic Aircraft," *Journal of Aircraft*, Vol. 37, No. 2, 2000, pp. 313–318.
doi:10.2514/2.2595
- [21] Raveh, D. E., Levy, Y., and Karpel, M., "Structural Optimization Using Computational Aerodynamics," *AIAA Journal*, Vol. 38, No. 10, Oct. 2000, pp. 1974–1981.
doi:10.2514/2.853
- [22] Levy, Y., "Numerical Simulation of Dynamically Deforming Aircraft Configurations Using Overset Grids," *Journal of Aircraft*, Vol. 38, No. 2, March–April 2001, pp. 349–354.
doi:10.2514/2.2768
- [23] Beam, R. M., and Warming, R. F., "An Implicit Finite-Difference Algorithm for Hyperbolic Systems in Conservation Law Form," *Journal of Computational Physics*, Vol. 22, No. 1, 1976, pp. 88–110.
doi:10.1016/0021-9991(76)90110-8
- [24] Steger, J. L., and Warming, R. F., "Flux Vector Splitting of the Inviscid Gasdynamic Equations with Applications to Finite-Difference Methods," *Journal of Computational Physics*, Vol. 40, No. 2, 1981, pp. 263–293.
doi:10.1016/0021-9991(81)90210-2
- [25] Batten, P., Leschziner, M. A., and Goldberg, U. C., "Average-State Jacobians and Implicit Methods for Compressible Viscous and Turbulent Flows," *Journal of Computational Physics*, Vol. 137, No. 1, 1997, pp. 38–78.
doi:10.1006/jcph.1997.5793
- [26] Liou, M.-S., and Steffen, C. J., "A New Flux Splitting Scheme," *Journal of Computational Physics*, Vol. 107, No. 1, 1993, pp. 23–39.
doi:10.1006/jcph.1993.1122
- [27] Liou, M.-S., "A Sequel to AUSM: AUSM⁺," *Journal of Computational Physics*, Vol. 129, No. 2, 1996, pp. 364–382.
doi:10.1006/jcph.1996.0256
- [28] Liou, M.-S., "A Sequel to AUSM, Part 2: AUSM⁺—Up," *Journal of Computational Physics*, Vol. 214, No. 1, 2006, pp. 137–170.
doi:10.1016/j.jcp.2005.09.020
- [29] Rossow, C. C., "A Flux-Splitting Scheme for Compressible and Incompressible Flows," *Journal of Computational Physics*, Vol. 164, No. 1, 2000, pp. 104–122.
doi:10.1006/jcph.2000.6586
- [30] Koren, B., "Upwind Schemes, Multigrid and Defect Correction for the Steady Navier–Stokes Equations," *Proceedings of the 11th International Conference in Numerical Methods in Fluid Dynamics*, edited by, D. L. Dwoyer, M. Y. Hussani, and, R. G. Voight, Springer–Verlag, Berlin, 1989, pp. 344–348.
- [31] Benek, J. A., Buning, P. G., and Steger, J. L., "A 3-D Chimera Grid Embedding Technique," *7th Computational Physics Conference*, Cincinnati, OH, AIAA Paper 1985-1523, July 1985.
- [32] Chan, W. M., and Buning, P. G., "Surface Grid Generation Methods for Overset Grids," *Computers and Fluids*, Vol. 24, No. 5, 1995, pp. 508–522.
doi:10.1016/0045-7930(95)00003-U
- [33] Karpel, M., Levy, Y., and Selitretnnik, E., "Aeroelastic CFD Time Simulation of a Morphing Wing-Body Configuration," *International Forum on Aeroelasticity and Structural Dynamics (IFASD)*, Council of European Aerospace Societies (CEAS) Paper IF-048, June 2007.
- [34] Harder, R. L., and Desmarais, R. N., "Interpolation Using Surface Splines," *Journal of Aircraft*, Vol. 9, No. 2, 1972, pp. 189–191.
doi:10.2514/3.44330
- [35] MSC/Nastran, Ver. 68, Basic Dynamic Analysis User's Guide, MacNeal–Schwendler Corp., Los Angeles, 2004.
- [36] Burden, R. R., and Faires, D. J., *Numerical Analysis*, 8th ed., Brooks/Cole, Boston, 2005, pp. 273–290.
- [37] Chung, T. J., *Computational Fluid Dynamics*, 2nd ed., Cambridge Univ. Press, New York, 2010, pp. 555–560.